Chemical Science

ROYAL SOCIETY OF CHEMISTRY

EDGE ARTICLE

View Article Online
View Journal

Cite this: DOI: 10.1039/d5sc09804a

All publication charges for this article have been paid for by the Royal Society of Chemistry

Dual-functional nanoengineering *via* molecular pillaring and conductive hybridization for high-performance aqueous zinc-ion batteries

Yajiang Wang,[ab] Xiudong Chen,*[a] Jin-Hang Liu,[a] Dongmei Qi,[ab] Hai-Yan Hu,[c] Huixiong Jiang,[a] Yan Huang,*[b] Ping Yan[a] and Yao Xiao *[cde]

Aqueous Zn-ion batteries (AZIBs) stand out as exceptionally promising energy storage devices owing to their superior safety, environmental benignity, and excellent electrochemical performance. However, high-performance cathode materials remain a challenge. Ammonium vanadate (NVO) nanosheets have garnered immense attention as potential AZIB cathodes due to their unique layered nanostructure, but repeated intercalation/extraction of ammonium ions induces severe nanoscale structural collapse, whereas the intrinsically low conductivity further hinders their real-world implementation. Herein, we introduce a nanoscale, dual-functional engineering strategy for NVO cathodes. This approach partially replaces interlayer NH_4^+ in NVO nanosheets with symmetric tetrahedral TMA^+ cations as "molecular pillars", and then hybridizes the modified nanosheets with graphene oxide (GO) to form a TNVO@GO nanocomposite. TMA^+ suppresses interlayer contraction at the nanoscale, alleviating lattice strain. GO hybridization constructs a continuous 2D nanoconductive network, accelerating electron transfer and preventing vanadium dissolution. Thus, TNVO@GO delivers a high specific capacity of 438.2 mAh g^{-1} at 0.2 A g^{-1}, with a capacity retention rate of 84.6% after 3000 cycles at 6.0 A g^{-1}. *In situ* and *ex situ* characterization further verified the reversible H^+/Zn^{2+} co-intercalation mechanism, in which TMA^+ and GO synergistically inhibit structural collapse and promote charge transfer. Furthermore, TNVO@GO based pouch cells exhibit stable performance under bending, confirming their practical application potential. This nanoscale dual-strategy engineering provides a feasible approach for optimizing vanadium-based cathodes and offers insights into the development of next-generation high-performance AZIBs.

Received 14th December 2025
Accepted 30th December 2025

DOI: 10.1039/d5sc09804a

rsc.li/chemical-science

1 Introduction

Aqueous zinc-ion batteries (AZIBs) emerged as a core option for grid scale energy storage due to cost competitiveness, superior safety, and environmental benignity, while their practical deployment is severely hindered by a lack of high-performance cathode materials. The poor structural stability and low electron conduction efficiency of cathode materials directly restrict the battery's capacity and cycle life.[1,2] Among the various candidates, vanadium-based materials have attracted attention due to their tunable structure and multivalent redox activity.[3–5] Commonly used vanadium oxides include VO_2,[6] V_2O_5,[7] $VOPO_4$,[8] VS_2,[9] and ammonium vanadate (NVO).[10] Compared with other vanadium-based cathodes, V_2O_5 faces a serious dissolution problem.[11] VO_2 exhibits limited capacity due to fewer active V sites.[12] $VOPO_4$ generally delivers low specific capacity owing to its inert PO_4^{3-} groups.[13] The VS_2 structure has poor stability and sluggish dynamics.[14] NVO possesses expanded interlayer spacing arising from the intercalated NH_4^+ in its layered structure, which provides unobstructed diffusion pathways for the rapid insertion and extraction of Zn^{2+} ions and effectively reduces the diffusion energy barrier. Meanwhile, NVO exhibits multivalent vanadium redox couples involving $V^{3+}/V^{4+}/V^{5+}$, which endows it with a high theoretical specific capacity. The intercalated NH_4^+ can also impart favorable structural flexibility to the layered architecture, which mitigates the lattice strain caused by Zn^{2+} insertion/extraction processes to a certain extent and thus maintains structural integrity. Furthermore, NVO can be prepared *via* a green low-temperature liquid-phase method, featuring a low preparation cost and facile synthetic procedure, which makes it a highly promising cathode material for AZIBs.[15]

[a]*School of Chemistry and Chemical Engineering, Jiangxi Province Engineering Research Center of Ecological Chemical Industry, Jiujiang University, Jiujiang 332005, China. E-mail: chenxd@jju.edu.cn*

[b]*State Key Laboratory of Organic-Inorganic Composites, Beijing University of Chemical Technology, Beijing 100029, China. E-mail: huangyan@mail.buct.edu.cn*

[c]*College of Chemistry and Materials Engineering, Wenzhou University, Wenzhou, Zhejiang 325035, China. E-mail: xiaoyao@wzu.edu.cn*

[d]*State Key Laboratory of Powder Metallurgy, Central South University, Changsha 410083, China*

[e]*State Key Laboratory of New Textile Materials and Advanced Processing, Wuhan Textile University, Wuhan 430200, China*

As a result, NVO materials exhibit a high application potential due to their unique layered structure and the characteristics of interlayered ammonium ions. However, repeated insertions and extractions of ammonium ions during the charge and discharge processes of NVO lead to lattice strain between layers, causing the layers to collapse and the cycle capacity to rapidly decline. Moreover, the inherent low electronic conductivity of NVO limits interfacial Zn^{2+} migration kinetics and charge transfer efficiency. Separately, severe vanadium dissolution from the NVO electrode into the electrolyte during cycling is another critical issue. These problems hinder the material from fully delivering its electrochemical performance.[16]

Various strategies have been developed to tackle these challenges, including metal cation intercalation,[17] organic molecular intercalation,[18] vacancy engineering,[19] and composite construction.[20] For layered vanadium oxides, intercalation stands out as a widely used engineering strategy. Metal ion intercalation reinforces the crystal structure and mitigates lattice strain-induced dissolution, while organic molecule intercalation enhances electrical conductivity. Therefore, organic cations, which combine the properties of both metal ions and organic molecules, offer the potential to combine the benefits of both types of intercalation.[21] When it comes to composite construction strategies, graphene oxide (GO) deserves special consideration. Due to its unique structure and functions, it perfectly counteracts the disadvantages of layered vanadium oxides.[22] In terms of enhancing electrical conductivity, GO possesses inherent high conductivity and a two-dimensional (2D) sheet-like structure, which enables the formation of a continuous electron transport network. This network can compensate for NVO's low electrical conductivity, ensuring efficient electron transfer during charge–discharge cycles. Additionally, the abundant oxygen-containing functional groups on the surface of the GO can form strong interfacial interactions with vanadium species in the oxide, effectively suppressing the dissolution of vanadium ions.[23]

Herein, we propose a dual-functional nanoengineering strategy that enhances both structural robustness and charge transport kinetics in NVO cathodes. To increase the interlayer spacing of NVO nanosheets, we introduced tetramethylammonium ions (TMA^+) as "molecular pillars" instead of traditional metal ion intercalators that form strong electrostatic interactions with Zn^{2+}. Due to its symmetric tetrahedral geometry, TMA^+ minimizes electrostatic interference with Zn^{2+} migration while effectively suppressing layer contraction and mitigating lattice strain. Meanwhile, we integrated GO into the NVO matrix to construct a two-dimensional conductive nanonetwork, thereby accelerating electron transfer, enhancing electrode stability, and preventing vanadium dissolution. Theoretical calculations and experimental results collectively demonstrate that this dual-nanoengineering approach stabilizes the NVO framework during cycling while significantly improving its electrical conductivity, resulting in high-performance AZIBs with an exceptional cycle life and rate. The TNVO@GO composite delivers a high specific capacity of 438.2 mAh g^{-1} at 0.2 A g^{-1}. At a high current density of 6.0 A g^{-1}, it retains 84.6% of its capacity after 3000 cycles. The reversible Zn^{2+} intercalation mechanism of NVO during electrochemical cycling has been confirmed *via in situ* Raman and *ex situ* XRD/XPS/HRTEM analyses. The interlayer framework stability and cycling performance are improved when ammonium ions are partially substituted. After compounding with GO, the material becomes even more electrically conductive. Using this nanoengineering strategy, NVO can be optimized using a simple, feasible approach, which will lead to a greater number of commercial applications.

2 Results and discussion

To address the collapse of the layered structure of pristine NVO caused by the intercalation/extraction of ammonium ions during cycling, as well as its low intrinsic electrical conductivity and severe vanadium dissolution, two modified materials (TNVO and TNVO@GO) were designed based on the dual strategy of organic cation intercalation and GO composite construction. Specifically, TNVO (TMA^+-intercalated NVO) is intended to utilize TMA^+ as "interlayer structural pillars" for stabilizing the layered framework, while TNVO@GO not only incorporates TMA^+ as "interlayer structural pillars" but also synergistically enhances electrical conductivity and suppresses vanadium dissolution through the unique properties of GO. Fig. S1 illustrates the TNVO@GO synthesis process. To confirm the rationality of this material design, density functional theory (DFT) calculations were performed (Fig. S2). The total density of states (DOS) of NVO, TNVO, and TNVO@GO is presented, respectively, depicting the electronic state distributions of constituent elements including V, O, N, and C. Notably, after introducing GO into TNVO@GO, the DOS near the Fermi level changes significantly (Fig. 1a–c). This synergistic modulation of the electronic structure by TMA^+ and GO is critical for enhancing the material's electrical conductivity and redox activity. The band structure-related characteristics show that the value corresponding to TNVO@GO (0.29 eV) is considerably lower than those of NVO (1.49 eV) and TNVO (1.38 eV), indicating that the introduction of GO modulates the electronic structure, thereby enhancing the electrical conductivity of TNVO@GO (Fig. 1d). Furthermore, orbital interactions were investigated *via* projected density of states (PDOS), while calculations of the d-band and p-band centers (Fig. 1e) were conducted to quantify the enhanced hybridization effect. Upon TMA^+ intercalation into TNVO, the V 3d band center shifts toward lower energy. This is likely attributed to electron transfer from V to positively charged TMA^+, as clearly visualized in the differential charge density maps. Regions of charge depletion around V atoms and charge accumulation on TMA^+ directly confirm the reduced electron density in V 3d orbitals, which attenuates electron–electron repulsion and thereby reduces their energy.[22] Notably, the unchanged Δ(d-p) confirms that TMA^+ does not impair d-p orbital hybridization strength or interfacial electron transfer efficiency, verifying its ability to modulate the local electronic state of V while maintaining the inherent structure and key electronic properties of the material. In contrast, Δ(d-p) exhibits a distinct change after the incorporation of GO, demonstrating that GO doping simultaneously

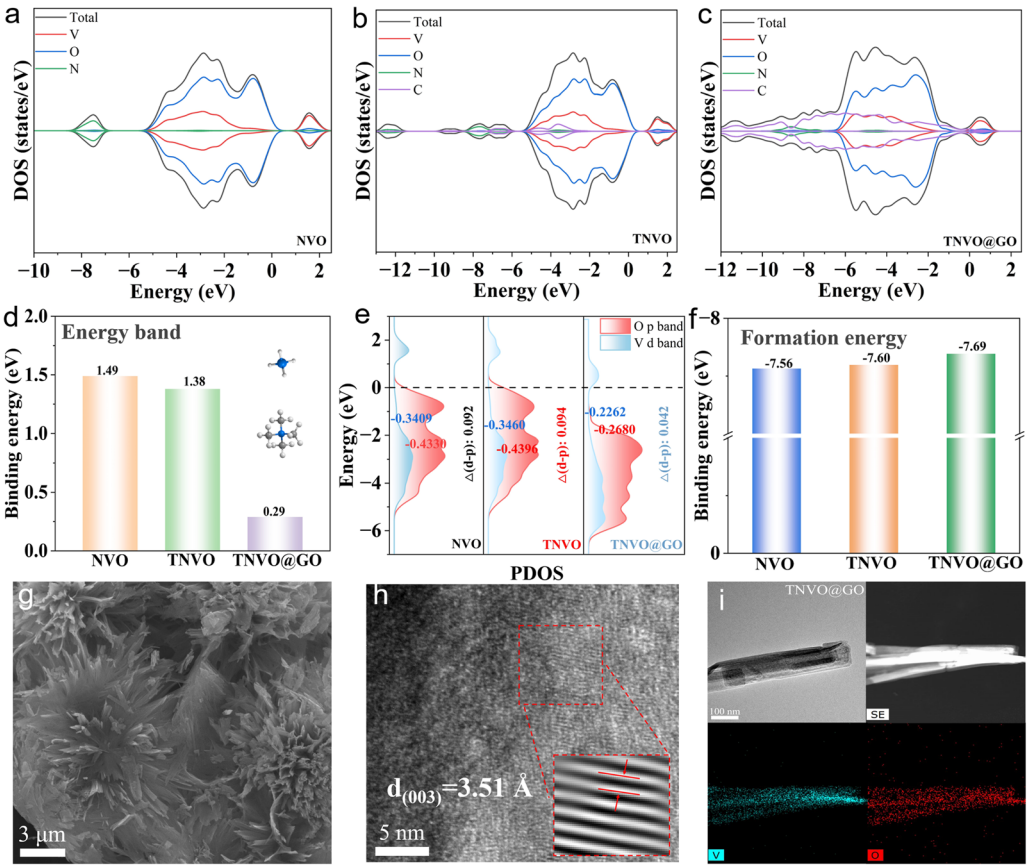

Fig. 1 DOS of (a) NVO, (b) TNVO, and (c) TNVO@GO. (d) Energy band of NVO, TNVO, and TNVO@GO. (e) PDOS analysis of d-p orbital hybridization of NVO, TNVO, and TNVO@GO. (f) Formation energy of NVO, TNVO, and TNVO@GO. (g) SEM and (h) TEM images of TNVO@GO. (i) HRTEM micrographs, HAADF image and matching elemental mappings of TNVO@GO.

enhances d-p orbital hybridization and interfacial electron transfer.[24] The formation energy histogram indicates that among these three samples, TNVO@GO exhibits the lowest formation energy (−7.69 eV, compared with −7.56 eV for NVO and −7.60 eV for TNVO), implying that TNVO@GO is thermodynamically more favorable and possesses higher structural stability (Fig. 1f). The differential charge density maps intuitively illustrate charge transfer and accumulation characteristics, with purple regions corresponding to charge accumulation and green regions indicating charge depletion (Fig. S3). In the TNVO@GO system, more pronounced charge redistribution can be observed at the interface, which confirms the efficient charge transfer between GO and TNVO. Electrochemical reactions are accelerated by intensifying interfacial interactions. Thus, this dual-engineering strategy can simultaneously address the issues of NVO at the structural and electronic levels.

Investigations into the effects of TMA^+ intercalation and the GO composite on the micromorphology of the materials involved systematic observations for NVO, TNVO, and TNVO@GO samples using scanning electron microscopy (SEM). The pristine NVO features a typical self-assembled cluster structure composed of nanosheets, with a nanosheet width of approximately 0.6 μm significantly larger than that of TNVO (Fig. S4). The reduced thickness of the nanosheets stems from the pillar effect of TMA^+ cations between layers. Electrostatic interactions and steric hindrance between their quaternary ammonium groups and vanadium-oxygen layers effectively suppress disordered nanosheet stacking.[25] The TNVO@GO nanocomposite exhibits a spherical morphology composed of interconnected ultrathin nanosheets, which maximizes exposure to electrochemically active sites but also facilitates rapid electron transfer by shortening transport pathways (Fig. 1g). TMA^+ intercalation constricts nanosheets, increasing specific surface area and exposing more active sites. TNVO possesses a specific surface area of 49.95 $m^2\ g^{-1}$, which is greater than that of NVO (42.52 $m^2\ g^{-1}$). The composite with GO connects the nanosheets closely, which results in a reduced specific surface area, consistent with the measured data (25.84 $m^2\ g^{-1}$) (Fig. S5a). However, TNVO@GO still features a mesopore-dominated pore structure, which can effectively facilitate electrolyte infiltration and shorten the diffusion distance of Zn^{2+} (Fig. S5b). The fine structure of TNVO@GO was characterized using transmission electron microscopy (TEM) and high-resolution transmission electron microscopy (HRTEM) (Fig. 1h and i). TNVO@GO features a stacking arrangement of ultrathin nanosheets, while HRTEM images clearly exhibit TNVO@GO lattice fringes (3.51 Å, assigned to the (003) crystal plane). Elemental mapping reveals a uniform elemental

distribution (Fig. 1i, S6 and S7). This structural regulation brings significant performance optimizations. The nanosheet structure of TNVO@GO facilitates ion diffusion, while the dense aggregates shorten electron transport paths, and the ordered stacking reduces Zn^{2+} diffusion distances. Collectively, these factors enhance electrode reaction kinetics, laying a microstructural foundation for improved electrochemical performance.

To analyze the crystalline phase composition and structural characteristics of the samples, multi-dimensional characterization techniques were employed. XRD (Fig. 2a and b) demonstrates that all diffraction peaks of NVO, TNVO, and TNVO@GO are perfectly matched with the standard card of $(NH_4)_2V_{10}O_{25}\cdot 8H_2O$ (PDF#26-0097), indicating that the intercalation of TMA^+ and incorporation of GO do not cause disruption to the bulk crystal phase. Notably, a slight shift of the (001) crystal plane is observed in TNVO and TNVO@GO, suggesting the successful intercalation of TMA^+ and resultant interlayer expansion, which facilitates Zn^{2+} intercalation.[26] The Rietveld refinement was performed further on TNVO@GO (Fig. 2a), and the refinement parameters are in good agreement with the experimental data and the theoretical fitting (Table S1). The molecular vibrational properties of the samples were analyzed using Raman and Fourier transform infrared (FTIR) spectroscopy (Fig. 2c and d). The peaks at 152.2, 264.5, 523.6, 694.1, and 1037.7 cm^{-1} are attributed to the –O–V–O–V bending vibration, V=O bending vibration, V_3–O stretching vibration, V_2–O stretching vibration, and V–O stretching vibration, respectively.[27] The increased intensity of each peak in TNVO is attributed to the more distinct crystalline structure induced by TMA^+ intercalation. However, the intensity decreases in TNVO@GO, which is due to the reduced crystallinity caused by GO incorporation, thereby obscuring the vanadium-related peaks.[28] Furthermore, in the Raman graphitization degree analysis, the D-band and G-band can be clearly observed, and this spectral feature further confirms the successful composite formation of GO (Fig. S8). In the FTIR spectrum of TNVO@GO, the peaks at 945.1 and 1402.2/1487.1 cm^{-1} are assigned to the characteristic peaks of C–N and C–H/C–C, respectively, which are absent in NVO, confirming the successful intercalation of TMA^+ and composite formation with GO.[29] Additionally, the bending vibration of V–O–V groups at 356.8 cm^{-1} indicates a more distinct crystalline structure, consistent with the Raman results.

Thermogravimetric (TG, Fig. 2e) analysis quantitatively characterizes the thermal evolution of the sample. The first stage weight loss is attributed to the loss of adsorbed water and partial bound water, while the second-stage weight loss

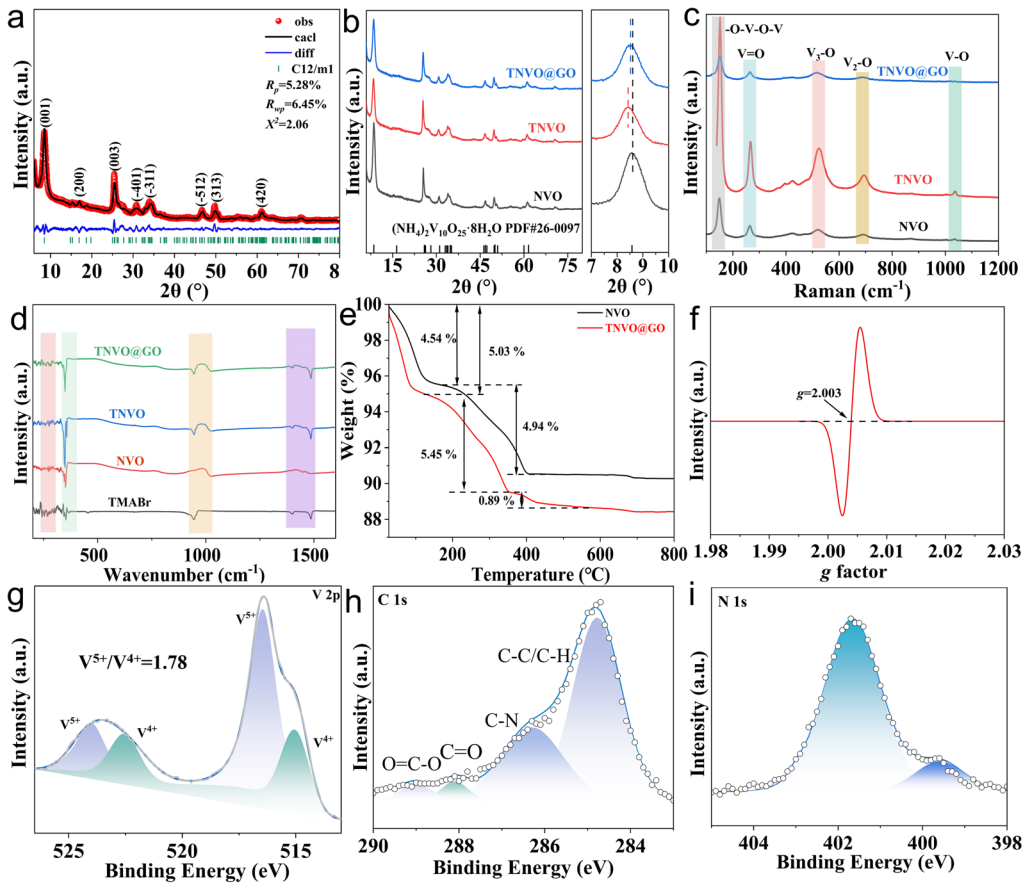

Fig. 2 (a) XRD patterns and the corresponding Rietveld refinement results of TNVO@GO. (b) XRD patterns of NVO, TNVO, and TNVO@GO samples. (c) Raman spectra of NVO, TNVO, and TNVO@GO. (d) FTIR spectra of NVO, TNVO, and TNVO@GO. (e) The TG curves of NVO and TNVO@GO. (f) The EPR spectra of TNVO@GO. The XPS spectra of (g) V 2p, (h) C 1s, and (i) N 1s.

corresponds to the loss of deeper bound water and organic cations. It can be observed herein that the weight loss rate of TNVO slows down, which is attributed to the higher thermal stability of TMA^+ compared to NH_4^+.[30] Furthermore, weight loss for TNVO@GO (5.45%) is greater than that for NVO (4.94%) and TNVO (4.84%), indicating that GO experiences weight loss at this stage (Fig. S9). TNVO@GO also exhibits a third stage, which corresponds to further weight loss for GO. TNVO@GO exhibits a characteristic signal at $g = 2.003$ in electron paramagnetic resonance (EPR), which can be attributed to unpaired electron spin resonance signals caused by oxygen vacancies.[31] The oxygen vacancies provide additional active sites for the rapid diffusion of Zn^{2+} and redox reactions, thereby accelerating ion diffusion and regulating redox kinetics. To further clarify the structural adjustments induced by TMA^+ intercalation and GO hybridization, an XPS analysis was performed (Fig. S10). In the V 2p spectrum (Fig. 2g), characteristic peaks of V^{5+} and V^{4+} are identified at 524.0/516.4 eV and 522.5/515.1 eV, with a V^{5+}/V^{4+} ratio of 1.78 (NVO, 2.49; TNVO, 1.38) (Fig. S11a and b).[32] The coexistence of these valence states reduces the electron transfer barrier, enabling faster redox reactions. The C 1s spectrum is deconvoluted into four constituent components, C–C/C–H (284.8 eV), C–N (286.3 eV), C═O (288.8 eV), and O═C–O (289.0 eV). Notably, the C–N peak at 286.3 eV provides direct evidence for TMA^+ intercalation (Fig. 2h).[33] More importantly, the presence of such features in TNVO@GO but not in NVO (Fig. S11c and d) indicates the formation of a coordination/hydrogen-bonding interface between graphene oxide and the vanadium matrix, which acts as a dual-functional bridge for both structural reinforcement and interfacial charge transfer, being conducive to enhancing electrochemical performance. In the N 1s spectrum of TNVO@GO, there are peaks at 399.5 and 401.7 eV assigned to N–C and NH_4^+, respectively (Fig. 2i and S12).[34] TMA^+ intercalation coincides with H_2O intercalation in the O 1s spectrum (Fig. S13).[35] Intercalated water acts as an interlayer lubricant, relieving the intense electrostatic interactions caused by intercalated Zn^{2+}.

For evaluating electrochemical performance, AZIB coin cells were assembled with NVO, TNVO, and TNVO@GO cathodes, metallic Zn anodes, 2 M $Zn(CF_3SO_3)_2$ aqueous electrolyte, and glass fiber separators. Multiple redox peak pairs are observed in TNVO@GO and control samples at 0.1 mV s^{-1}, indicating multivalent valence transitions in vanadium (Fig. 3a and S14). The redox peaks at 1.11/0.99 V and 0.75/0.62 V correspond to V^{5+}/V^{4+} and V^{4+}/V^{3+} redox couples, respectively. Significantly, a pair of faint peaks at 1.44/1.21 V is linked to NH_4^+ intercalation/extraction. Hence, TMA^+ with a larger radius only replaces a fraction of ammonium ions. However, the remaining ammonium ions can still be intercalated/extracted. Besides, the redox features at 0.98/0.79 V and 0.52/0.40 V are associated with the electrochemical processes of $Zn_3(OH)_2V_2O_7\cdot 2H_2O$ (ZHVO).[15,36] These observations collectively demonstrate complex redox chemistry involving both vanadium valence changes and ionic intercalation mechanisms in the studied electrode systems. It can be seen that the redox platform is consistent with CV at a GCD of 0.2 A g^{-1} (Fig. 3b). A comparison of the energy and power densities of previously reported vanadium-based oxide cathodes in the Ragone plot revealed that TNVO@GO exhibits an energy density of 314 Wh kg^{-1} at 140 W kg^{-1} and 170 Wh kg^{-1} at 2426 W kg^{-1}, which ranks relatively high among the reported materials (Fig. 3c and Table S2).[37–48] Cycling tests were performed on different cathode materials. TNVO@GO samples exhibit a high initial discharge specific capacity of 438.2 mAh g^{-1} at 0.2 A g^{-1}, and can still retain a specific capacity of 305.7 mAh g^{-1} after 50 cycles (Fig. S15a). In contrast, the NVO cathode shows an initial specific capacity of only 364.3 mAh g^{-1} and retains 52.7% of its capacity under the same conditions. Even at a current density as high as 6.0 A g^{-1}, the TNVO@GO electrode still maintains excellent performance (Fig. 3d). After 3000 cycles, its capacity retention rate compared to the initial capacity is 84.6%, which is superior to that of NVO (60.0% after 2400 cycles) and TNVO (80.2% after 2400 cycles). Additionally, the TNVO@GO cathode demonstrates better rate capability than NVO and TNVO cathodes. At current densities of 0.2, 0.5, 1.0, 2.0, 4.0, 6.0, 1.0, 0.5 and 0.2 A g^{-1}, the average discharge specific capacities of the TNVO@GO cathode are 412.8, 396.7, 383.8, 368.5, 343.1, 318.5, 383.1, 391.6 and 392.2 mAh g^{-1}, respectively. When the current density is rapidly restored to 0.2 A g^{-1}, the discharge specific capacity can still reach 392.2 mAh g^{-1} (equivalent to 95.0% recovery of the initial capacity), indicating excellent reversibility and stability (Fig. 3e and S15b). Intercalation and extraction of ammonium ions can lead to structural collapse of NVO. TMA^+ ions exert a supporting effect between the layers, rendering the interlayer framework more stable and thereby inhibiting structural collapse.[26] This results in the retention of the structural integrity of ammonium vanadate-based materials during long-term cycling. Further self-discharge tests were performed to explore their charge storage capability and stability. In the self-discharge test, after 48 h of resting, the coulombic efficiency of TNVO@GO reached 85.3%, which is significantly superior to those of NVO (80.8%) and TNVO (82.3%) (Fig. S16). This result demonstrates that TNVO@GO possesses excellent structural and electrochemical stability, thus exhibiting outstanding long-term charge retention capability at rest. Such superior performance is not only derived from the structural stability of the material, but also benefits from the synergistic effect of multiple favorable factors. Specifically, the TMA^+ pillar effect not only enhances TNVO@GO structural stability and inhibits lattice collapse during the self-discharge process, but also suppresses the dissolution of vanadium species and the occurrence of irreversible interfacial side reactions. In addition, the conductive network constructed by GO effectively reduces interfacial charge transfer resistance. It also alleviates irreversible capacity loss induced by interfacial charge accumulation. These multiple positive effects endow TNVO@GO with excellent self-discharge performance. In electrochemical impedance spectroscopy (EIS) measurements, it was observed that the impedance decreased significantly after one cycle of CV (Fig. S17). The charge transfer resistance of TNVO@GO was smaller than that of pristine NVO and TNVO, indicating superior charge transfer kinetics.[49] This perfectly coincides with the trend of conductivity enhancement revealed by theoretical calculations. The optimized electronic structure essentially elevates the intrinsic electronic

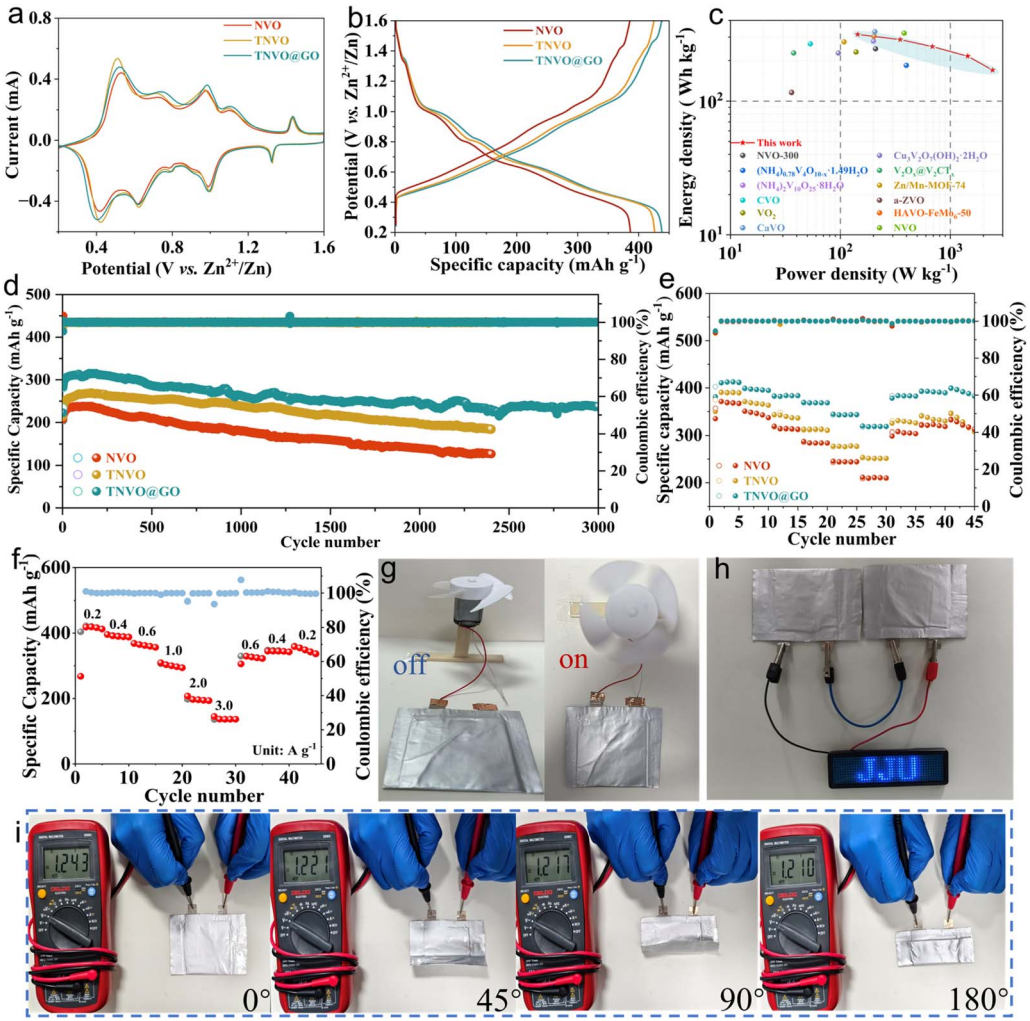

Fig. 3 (a) CV curves of NVO, TNVO, and TNVO@GO at 0.1 mV s^{-1}. (b) GCD curves of NVO, TNVO, and TNVO@GO at 0.2 A g^{-1}. (c) Ragone plots *versus* other cathode materials. (d) Long-term cycling performance at a current density of 6.0 A g^{-1}. (e) Rate performance at current densities ranging from 0.2 to 6.0 A g^{-1}. (f) Rate performance of TNVO@GO pouch-cell batteries. (g) The TNVO@GO-based pouch-cell batteries power a small fan (on–off switch demonstrated). (h) LED lamp powered by two pouch-cell batteries in series. (i) The open circuit voltage of the TNVO@GO pouch-cell battery at 0°, 45°, 90°, and 180° bending states.

conductivity of TNVO@GO, leading to a remarkable reduction in charge transfer resistance.

The pouch-cell zinc-ion batteries were fabricated using TNVO@GO as the cathode, zinc foil as the anode, glass fiber as the separator, and 2 M $Zn(CF_3SO_3)_2$ as the electrolyte. As shown in the GCD profiles (Fig. S18), the pouch cell maintained well-defined redox platforms without significant alteration. Electrochemically, the battery delivered an initial specific capacity of 346.2 mAh g^{-1} at 0.7 A g^{-1} and retained 177.8 mAh g^{-1} after 80 cycles, demonstrating robust cycling stability (Fig. S19). Its rate capability was also excellent, with average specific capacities of 419.1, 390.0, 300.2, 196.2, 136.6, 120.0, 326.7, 344.7, and 348.9 mAh g^{-1} at sequentially varying current densities from 0.2 to 3.0 and back to 0.2 A g^{-1}, indicating high reversibility (Fig. 3f). To demonstrate the battery's practical performance, it was used to power an electric fan. The fan operated stably when switched on, visually confirming its potential for portable electronics (Fig. 3g). Furthermore, two serially connected pouch cells successfully lit a "JJU" LED panel, underscoring their real-world applicability (Fig. 3h). The cell also exhibited excellent mechanical flexibility, with its open-circuit voltage only decreasing minimally from 1.243 V to 1.210 V ($\Delta V = 0.033$ V) after folding at angles from 0° to 180°, thus maintaining structural integrity under deformation (Fig. 3i and S20).

For an in-depth insight into the electrochemical kinetic properties of the TNVO@GO composite and its control samples, CV was systematically performed in this study over a scan rate range of 0.2 to 1.0 mV s^{-1} (Fig. 4a–d and S21). With increasing scan rates, CV curves maintain a similar shape with slight peak potential shifts. This indicates rapid charge transfer kinetics and low electrochemical polarization of the electrode reaction. For peaks 1–6 of TNVO@GO, the correlation between the peak current and scan rate was 0.85, 1.09, 0.86, 0.95, 0.96 and 0.84 (Fig. 4e). These results revealed that the zinc storage process is co-governed by diffusion control and pseudocapacitive behavior at the tested scan rates, and pseudocapacitive behavior is

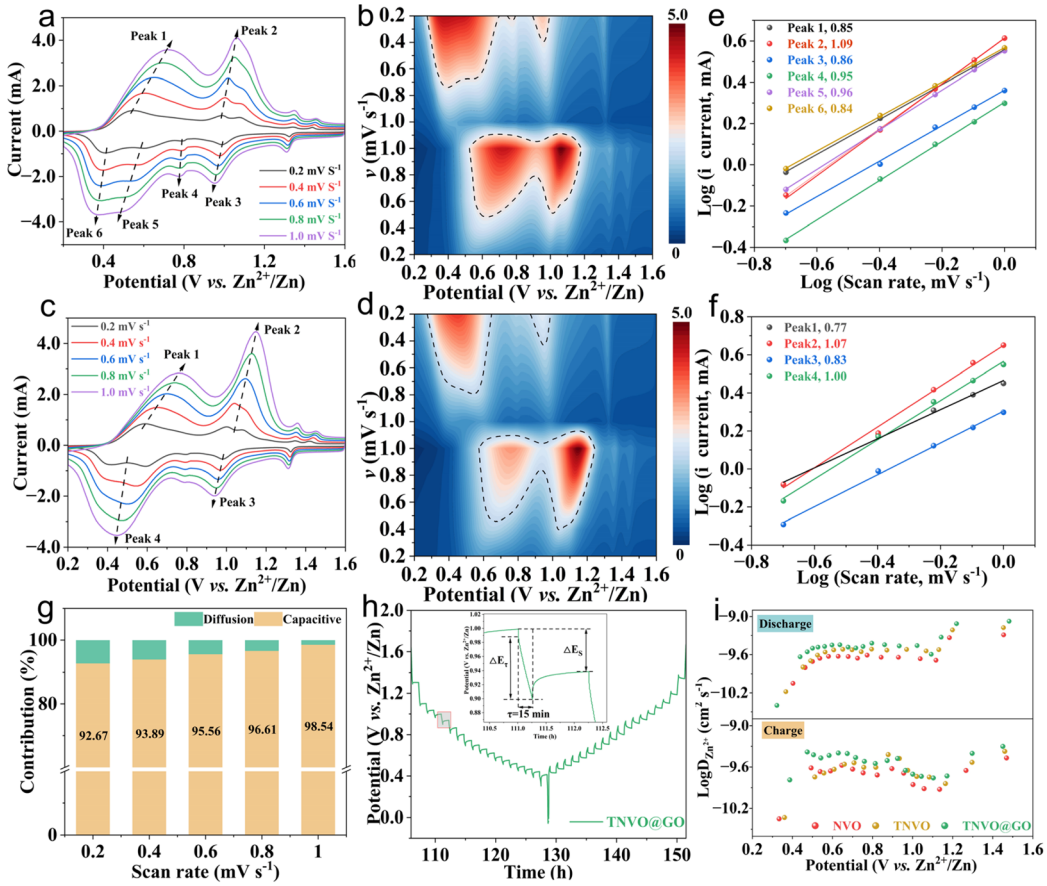

Fig. 4 (a and b) CV curves of TNVO@GO at different scan rates. (c and d) CV curves of NVO at different scan rates. (e and f) log(peak current) *vs.* log(scan rate) plots for each redox peak of TNVO@GO and NVO. (g) Bar graph of capacitive controlled and diffusion-controlled capacity contribution ratios for TNVO@GO at different scan rates. (h) GITT curves of TNVO@GO. (i) The calculated Zn^{2+} diffusion coefficients (D_{Zn}^{2+}) of NVO, TNVO, and the TNVO@GO electrode in the charge/discharge process.

dominant. Compared with NVO, TNVO@GO has an increased contribution of pseudocapacitance (Fig. 4f), indicating a faster diffusion rate.[50] The pseudocapacitance contribution in TNVO@GO gradually increased with the increase in scan rate, reaching 98.2% at 1.0 mV s^{-1} (Fig. 4g, S22 and 23), which was higher than that of HVO and TNVO. Such a high pseudocapacitive contribution, combined with rapid charge transfer kinetics, endows the TNVO@GO composite with excellent fast reaction kinetics. This is mainly attributed to the introduction of GO, which enhances the electrode's electrical conductivity.[51] Meanwhile, the constructed conductive network and nanostructure also shorten ion diffusion pathways and improve diffusion kinetics. To verify the ion transport kinetics, the Zn^{2+} diffusion coefficient in TNVO@GO was determined to be 10^{-9}–10^{-10} cm^2 s^{-1} *via* the galvanostatic intermittent titration technique (GITT) (Fig. S24), indicating its rapid ion diffusion capability (Fig. 4h and i).[52] This can be attributed to TMA^+ pre-intercalation, which enlarges the interlayer spacing and reduces the Zn^{2+} diffusion energy barrier. Meanwhile, the two-dimensional ion channels constructed by GO shorten Zn^{2+} diffusion pathways and accelerate interfacial ion migration.

The reversible zinc storage mechanism of TNVO@GO was elucidated through multi-scale *in situ* and *ex situ* characterization studies. The peaks at 277.6 cm^{-1} (V=O) and 520.1 cm^{-1} (V–O–V) decreased significantly during discharge and recovered to the initial intensity after charging in *in situ* Raman testing (Fig. 5a and b). The intensity of the peak at 1037.7 cm^{-1} (V–O) weakened upon discharge and recovered after charging, indicating the occurrence of stretching of V–O bonds. Such lattice contraction can inhibit the structural collapse caused by Zn^{2+} intercalation.[53] The structural evolution of TNVO@GO during charge–discharge cycles was studied using *ex situ* XRD (Fig. 5c). Within the 2θ range of 5–80°, its characteristic peaks remained stable throughout the entire cycling process, which demonstrates the excellent structural stability of the material. Discharge led to a shift of the $2\theta = 34°$ diffraction peak to lower angles, arising from Zn^{2+} intercalation-induced interlayer spacing expansion. Recovering peak positions post-charging confirmed the high reversibility of Zn^{2+} intercalation/extraction. Notably, new peaks at 2θ = 12.2°, 16.4°, and 59.0° in the discharged state ($Zn_3(OH)_2V_2O_7 \cdot 2H_2O$, PDF#87-0417) indicate OH^- involvement in the reaction. The complete disappearance of these ZHVO peaks during charging confirms the reversible decomposition of this active intermediate phase rather than the formation of irreversible byproducts. Moreover, the diffraction peak intensity at 2θ = 8–9°

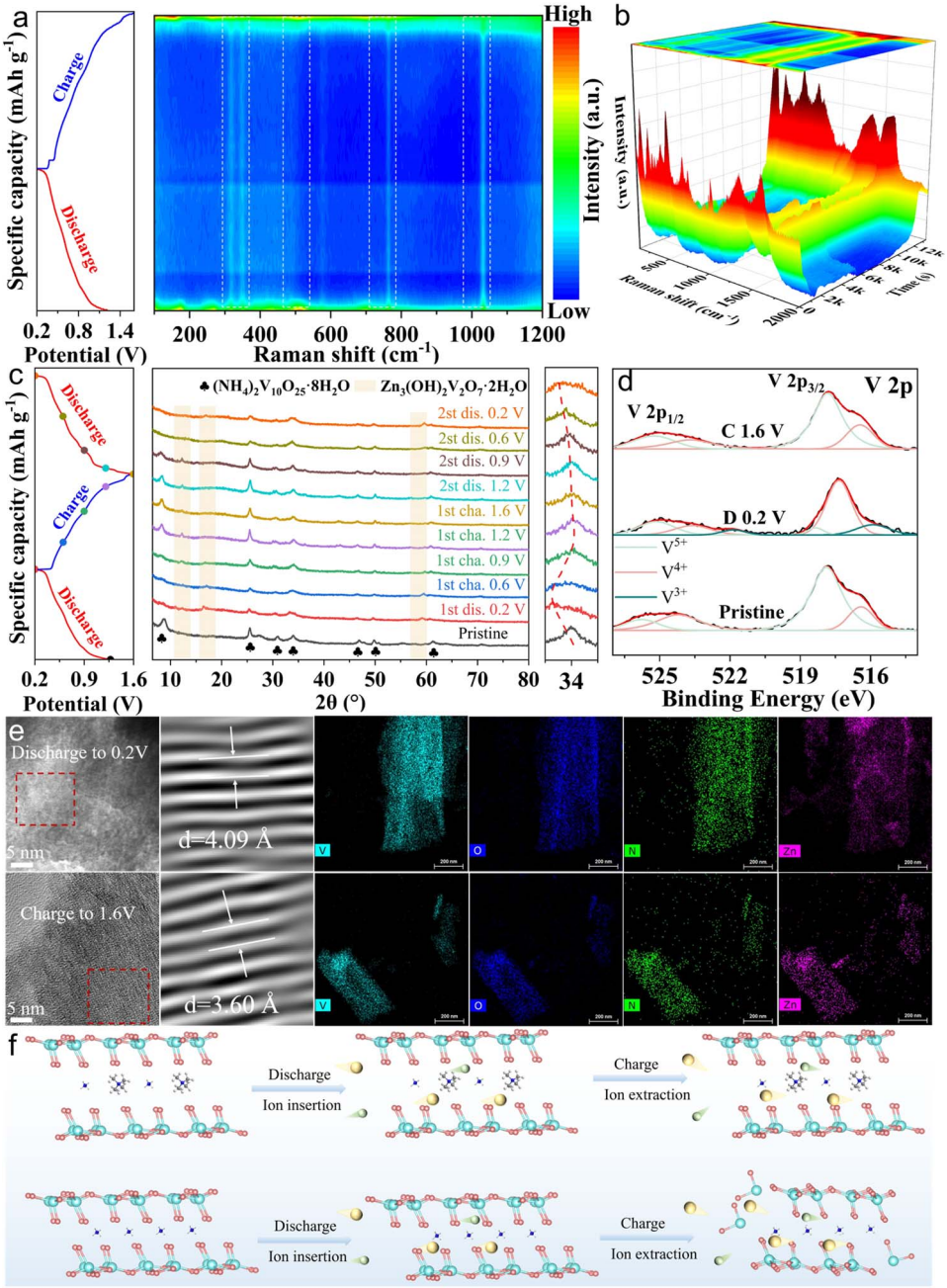

Fig. 5 (a) GCD curves and *in situ* Raman spectra of TNVO@GO during the charge/discharge cycling process. (b) The 3D color-mapped surface plot with a projection of the *in situ* Raman pattern. (c) TNVO@GO electrodes in various charging/discharging stages and *ex situ* XRD patterns. (d) *Ex situ* XPS spectra of V 2p of TNVO@GO electrodes. (e) HRTEM image and corresponding EDS elemental mapping at discharge to 0.2 V and charge to 1.6 V after the first cycle of TNVO@GO electrodes. (f) Schematic diagram of the energy storage mechanism and structure.

decreases upon discharge and recovers with a low angle shift during charging (Fig. S25), which indicates a reduction in crystalline order during Zn^{2+} intercalation. This structural evolution can effectively alleviate the electrostatic repulsion induced by Zn^{2+} intercalation, while the reversible formation and decomposition of the ZHVO intermediate phase further buffers the lattice strain of the electrode, synergistically facilitating the reversible migration of Zn^{2+} and enhancing the structural integrity of the cathode.[54,55] This observation reveals a reduction in crystalline order during the Zn^{2+} insertion process, thereby effectively alleviating the electrostatic repulsion induced by ion insertion.[54,55] The changes in bonds observed in *in situ* Raman spectroscopy are consistent with the reversible interlayer spacing variations detected by *ex situ* XRD, collectively confirming the reversible zinc storage mechanism.

To further investigate the changes in the valence states of elements involved in the zinc storage mechanism, *ex situ* XPS measurements were conducted (Fig. S26a). V 2p measurements reveal valence state variations of vanadium that correlate with the ion migration process (Fig. 5d). Specifically, when

discharged to 0.2 V, the characteristic peak of V^{3+} emerges, accompanied by a decreased intensity of the V^{5+} peak and an increased intensity of the V^{4+} peak. Upon charging to 1.6 V, all valence state characteristic peaks of V revert to their initial states. These changes directly correspond to the intercalation and extraction of Zn^{2+}, respectively, confirming that Zn^{2+} migration is closely coupled with vanadium redox reactions. Further insights into the intercalation mechanism are provided by O 1s measurements (Fig. S26b). In the discharged state, the intensified peak corresponding to H_2O indicates that Zn^{2+} intercalates in the form of $[Zn(H_2O)_6]^{2+}$. Concomitantly, the intercalation weakens V–O bonds, as evidenced by the diminished intensity of the V–O-related peak. Upon charging, V–O bonds recover (reflected by the restored V–O peak intensity). However, the H_2O peak shows no significant decrease, an observation that, like the residual Zn, can be attributed to ZHVO formation. Furthermore, discharge to 0.2 V induces a marked increase in Zn 2p peaks, confirming successful Zn^{2+} intercalation (Fig. S26c). By charging to 1.6 V, the Zn peak intensity is reduced, suggesting Zn extraction. Notably, some Zn remains in the material as a result of the formation of ZHVO.[28,36]

In addition, due to the co-insertion/extraction of H^+/Zn^{2+}, changes in lattice spacing were observed in HRTEM images (Fig. 5e). EDS mapping reveals a variation in Zn signal intensity, confirming reversible Zn^{2+} insertion/extraction that is well consistent with *ex situ* XPS results. It can be clearly observed that ZHVO has already formed in the initial state and remains stably present throughout subsequent charge–discharge processes in *ex situ* SEM (Fig. S27). For the TNVO@GO sample, its microstructure exhibits regular changes with charge–discharge states, and when discharged to 0.2 V, the sample presents a compact block-like structure. After charging to 1.6 V, it does not form a highly dense structure. Instead, numerous voids are observed. This phenomenon is attributed to the presence of GO, which effectively inhibits the excessive formation of ZHVO and thus prevents the material from being encapsulated by ZHVO. The experimental results reveal the H^+/Zn^{2+} co-intercalation energy storage mechanism (Fig. 5f); TMA^+ ions stabilize the layered structure, whereas GO mitigates vanadium dissolution, conferring superior electrochemical performance.

3 Conclusion

Herein, we demonstrate a nanoscale dual-engineering strategy for ammonium vanadate (NVO) nanosheet cathodes, where partial substitution of interlayer NH_4^+ with tetramethylammonium ions (TMA^+) acts as molecular pillars to expand the interlayer spacing, and GO wrapping constructs a continuous 2D nanoconductive network. In AZIBs, this nanoscale synergy stabilizes the layered host structure against irreversible collapse and accelerates electron transport kinetics. Hence, this strategy delivers an initial specific capacity of 438.2 mAh g^{-1} at 0.2 A g^{-1} and superior long-term cycling stability, with 84.6% capacity retention after 3000 cycles at 6.0 A g^{-1} (high current density). Combined *in situ* and *ex situ* characterization studies clearly verify the H^+/Zn^{2+} co-intercalation mechanism, and the performance demonstrated in flexible batteries confirms the translational potential of this material in wearable energy storage systems. These findings provide insights into advanced cathode engineering strategies for next-generation AZIBs.

Author contributions

Yajiang Wang: data curation, writing-original draft. Xiudong Chen: conceptualization, project administration, funding acquisition, writing-review & editing. Jin-Hang Liu: supervision, formal analysis. Dongmei Qi: conceptualization, supervision. Hai-Yan Hu: investigation, formal analysis. Huixiong Jiang: formal analysis, project administration. Yan Huang: data curation, formal analysis, project administration. Ping Yan: conceptualization, supervision. Yao Xiao: supervision, visualization, formal analysis, writing-review & editing.

Conflicts of interest

There are no conflicts of interest to declare.

Data availability

Essential data are fully provided in the main text and supplementary information (SI). Supplementary information is available. See DOI: https://doi.org/10.1039/d5sc09804a.

Acknowledgements

This work was supported by the National Natural Science Foundation of China (22163003), the Jiangxi Province Double Thousand Plan (jxsq2023201091), the Jiangxi Provincial Natural Science Foundation (20232BAB204024 and 20232BAB203024), the Science and Technology Project of the Jiangxi Provincial Department of Education (GJJ2401837 and GJJ2501824), the Jiujiang Science and Technology Project (2025_00174, 2025_00670), the Open Research Fund of the State Key Laboratory of Powder Metallurgy, Central South University (Sklpm-KF-2025018), and State Key Laboratory of New Textile Materials and Advanced Processing, Wuhan Textile University (FZ2025008).

References

1 R. F. Service, *Science*, 2021, **372**, 890–891.
2 G. Zampardi and F. Mantia, *Nat. Commun.*, 2022, **13**, 687.
3 C. Qiu, H. Huang, M. Yang, L. Xue, X. Zhu, Y. Zhao, M. Ni, T. Chen and H. Xia, *Energy Storage Mater.*, 2024, **72**, 103736.
4 T. Lv, Y. Peng, G. Zhang, S. Jiang, Z. Yang, S. Yang and H. Pang, *Adv. Sci.*, 2023, **10**, 2206907.
5 R. Sinha, X. Xie, Y. Yang, Y. Li, Y. Xue, P. Wang and Z. Li, *Adv. Energy Mater.*, 2025, **15**, 2404815.
6 Q. He, T. Hu, Q. Wu, C. Wang, X. Han, Z. Chen, Y. Zhu, J. Chen, Y. Zhang, L. Shi, X. Wang, Y. Ma and J. Zhao, *Adv. Mater.*, 2024, **36**, 2400888.
7 H. Lin, J. Gong, Y. Guan, Z. Shao, C. Tang, H. Yao, W. He and G. Du, *Chem. Eng. J.*, 2025, **524**, 169244.

8 Y. Lin, J. Meng, P. Hei, Y. Wang, B. Li, X. Sun, Y. Song and X.-X. Liu, *Adv. Funct. Mater.*, 2025, **35**, 2415639.
9 M. Yang, Y. Lin, P. Chen, M. Lai, J. Zhu, G. Li, M. Chen, Y. Wang, M. Chuai, J. Chen, G. Chai, H. Mi, L. Sun, C. He, D. Ma and P. Zhang, *Angew. Chem., Int. Ed.*, 2025, e202510907.
10 Q. Zong, W. Du, C. Liu, H. Yang, Q. Zhang, Z. Zhou, M. Atif, M. Alsalhi and G. Cao, *Nano-Micro Lett.*, 2021, **13**, 116.
11 J. Gong, B. Zhu, Y. Guan, H. Lin, Z. Shao, C. Tang, H. Yao, G. Du and W. He, *Chem. Commun.*, 2025, **61**, 18136–18139.
12 B. Wan, Y. Wang, X. Chen, C. Zhan, H. Jiang, J.-H. Liu, Y. Gao, X. Jiang, X. Cao, H. Zhang, S.-X. Dou and Y. Xiao, *Chem. Sci.*, 2025, **16**, 8217–8239.
13 Y. Wu, Q. Zong, C. Liu, Y. Zhuang, D. Tao, J. Wang, J. Zhang, Q. Zhang and G. Cao, *Small*, 2023, **19**, 2303227.
14 M. Yang, Z. Wang, H. Ben, M. Zhao, J. Luo, D. Chen, Z. Lu, L. Wang and C. Liu, *J. Colloid Interface Sci.*, 2022, **607**, 68–75.
15 S. Yao, Y.-G. Sun, Z. Cui and G.-J. He, *Rare Met.*, 2025, **44**, 6081–6091.
16 K. Fang, Y.-L. Liu, P. Chen, H. Zhang, D. Fang, H.-Y. Zhang, Z. Wei, L. Ding, G.-G. Wang and H. Y. Yang, *Nano Energy*, 2023, **114**, 108671.
17 Y. Guan, J. Gong, H. Lin, Z. Shao, C. Tang, H. Yao, W. He and G. Du, *J. Colloid Interface Sci.*, 2026, **703**, 139154.
18 S. Kong, Y. Li, X. Zhang, Z. Xu, X. Wang, Y. Feng, W. Gong, C. Liu, K. Tian and Q. Li, *Small*, 2023, **19**, 2304462.
19 L. Zhang, D. Fang, F. Wang, J. Yi, M. Wang, T. Hu and Y. Zhao, *Chem.–Eng. J.*, 2025, **506**, 159920.
20 W. Nie, J. Sun, S. Xu, L. Liu, P. Sun, Q. Hu, X. Zheng, Y. Sun, Z. Li, Z. Xu and H. Jia, *Chem.–Eng. J.*, 2023, **478**, 147385.
21 H. Liu, H. Niu, W. Huang, T. Shen, C. Li, C. Chang, M. Yang, C. Gao, L. Yang, Q. Zong, Y. Pei, G. Cao and C. Liu, *ACS Energy Lett.*, 2024, **9**, 5492–5501.
22 F. Qiao, W. Zhang, J. Wang, J. Cheng, J. Li, L. Cui, L. Zhou and Q. An, *Angew. Chem., Int. Ed.*, 2025, **64**, e202514410.
23 Z. Qin, G. Han, Y. Yang, S. Hao, L. Yu, Y. Lin, Y. Li, R. Lv, W. Shen, F. Kang and Z.-H. Huang, *Chem.–Eng. J.*, 2025, **513**, 162952.
24 R. Luo, Q. Yang, L. Sun, Y. Liu, L. Li, Y. Lei and W. Shi, *Adv. Mater.*, 2025, e16093.
25 Y. Tong, Y. Zang, S. Su, Y. Zhang, J. Fang, Y. Yang, X. Li, X. Wu, F. Chen, J. Hou and M. Luo, *J. Energy Chem.*, 2023, **77**, 269–279.
26 K. Wang, S. Li, X. Chen, J. Shen, H. Zhao and Y. Bai, *ACS Nano*, 2024, **18**, 7311–7323.
27 X. Jia, C. Liu, Z. Wang, D. Huang and G. Cao, *Nano-Micro Lett.*, 2024, **16**, 129.
28 D. Jia, Z. Shen, Y. Lv, Z. Chen, H. Li, Y. Yu, J. Qiu and X. He, *Adv. Funct. Mater.*, 2024, **34**, 2308319.
29 Q. Zong, Y. Zhuang, C. Liu, Q. Kang, Y. Wu, J. Zhang, J. Wang, D. Tao, Q. Zhang and G. Cao, *Adv. Energy Mater.*, 2023, **13**, 2301480.
30 D. Xin, X. Zhang, Z. Zhang, J. Sun, Q. Li, X. He, R. Jiang, Z. Liu and Z. Lei, *Small*, 2024, **20**, 2403050.
31 S. Li, X. Xu, W. Chen, J. Zhao, K. Wang, J. Shen, X. Chen, X. Lu, X. Jiao, Y. Liu and Y. Bai, *Energy Storage Mater.*, 2024, **65**, 103108.
32 S. Zhao, S. Wang, J. Guo, L. Li, C. Li, Y. Sun, P. Xue, D. Wu, L. Wei, Y. Wang and Q. Zhang, *Adv. Funct. Mater.*, 2023, **33**, 2305700.
33 G.-L. Liu, T. Zhang, X.-J. Li, R.-P. Cao, J.-K. Shen, D.-L. Guo, N.-T. Wu, W.-W. Yuan, A. Cao and X.-M. Liu, *Rare Met*, 2023, **42**, 3729–3740.
34 Z. Song, Y. Zhao, A. Zhou, H. Wang, X. Jin, Y. Huang, L. Li, F. Wu and R. Chen, *Small*, 2024, **20**, 2305030.
35 D. Zhang, J. Cao, C. Yang, K. Lolupiman, W. Limphirat, X. Wu, X. Zhang, J. Qin and Y. Huang, *Adv. Energy Mater.*, 2025, **15**, 2404026.
36 H. Liu, X. Hou, Q. Zhang, W. Peng, Y. Li and X. Fan, *Adv. Energy Mater.*, 2025, **15**, 2406171.
37 Y. Zheng, C. Tian, Y. Wu, L. Li, Y. Tao, L. Liang, G. Yu, J. Sun, S. Wu, F. Wang, Y. Pang, Z. Shen, Z. Pan, H. Chen and J. Wang, *Energy Storage Mater.*, 2022, **52**, 664–674.
38 L. Zhang, X. Zhu, M. Wang, D. Fang and J. Yi, *Chem.–Eng. J.*, 2024, **498**, 155645.
39 T. Wei, Q. Li, G. Yang and C. Wang, *J. Mater. Chem. A*, 2018, **6**, 20402.
40 C. Xia, J. Guo, P. Li, X. Zhang and H. N. Alshareef, *Angew. Chem., Int. Ed.*, 2018, **57**, 3943–3948.
41 C. Liu, W. Xu, C. Mei, M. Li, W. Chen, S. Hong, W. Kim, S. Lee and Q. Wu, *Adv. Energy Mater.*, 2021, **11**, 2003902.
42 D. Narsimulu, R. Shanthappa, H. Bandi and J. S. Yu, *ACS Sustainable Chem. Eng.*, 2023, **11**, 12571–12582.
43 L. Chen, Z. Yang, J. Wu, H. Chen and J. Meng, *Electrochim. Acta*, 2020, **330**, 135347.
44 R. Venkatkarthick, N. Rodthongkum, X. Zhang, S. Wang, P. Pattananuwat, Y. Zhao, R. Liu and J. Qin, *ACS Appl. Energy Mater.*, 2020, **3**, 4677–4689.
45 S. Deng, B. Xu, J. Zhao, C. W. Kan and X. Liu, *Angew. Chem., Int. Ed.*, 2024, **63**, e202401996.
46 B. Sambandam, V. Soundharrajan, S. Kim, M. H. Alfaruqi, J. Jo, S. Kim, V. Mathew, Y.-k. Sun and J. Kim, *J. Mater. Chem. A*, 2018, **6**, 3850–3856.
47 Y. Zhang, Q. Li, W. Feng, H. Yue, S. Gao, Y. Su, Y. Tang, J. Wu, Z. Zhang, Y. Zhang, M. Shakouri, H. Chen and H. Pang, *Angew. Chem., Int. Ed.*, 2025, **64**, e202501728.
48 Y. Xu, G. Fan, P. Sun, Y. Guo, Y. Wang, X. Gu, L. Wu and L. Yu, *Angew. Chem., Int. Ed.*, 2023, **62**, e202303529.
49 D. Li, Z. Ye, H. Ding, J. Li, H. Huang, Z. Yang, J. Su, J. Zhu and W. Zhang, *Energy Storage Mater.*, 2024, **71**, 103635.
50 F. Wan, Z. Hao, S. Wang, Y. Ni, J. Zhu, Z. Tie, S. Bi, Z. Niu and J. Chen, *Adv. Mater.*, 2021, **33**, 2102701.
51 M. Li, M. Liu, Y. Lu, G. Zhang, Y. Zhang, Z. Li, Q. Xu, H. Liu and Y. Wang, *Adv. Funct. Mater.*, 2024, **34**, 2312789.
52 J. Guo, B. He, W. Gong, S. Xu, P. Xue, C. Li, Y. Sun, C. Wang, L. Wei, Q. Zhang and Q. Li, *Adv. Mater.*, 2024, **36**, 2303906.
53 W. Kang, B. Zhang, Z. Wang, Z. Zhang, M. Niu, X. An, Z. Mou, X. Fan, X. Hu, B. Xi and S. Xiong, *J. Energy Chem.*, 2024, **94**, 608–617.
54 F. Zhang, Y. Kang, X. Zhao, H. Li, H. Dong, W. Wei, Y. Sang, H. Liu and S. Wang, *Adv. Funct. Mater.*, 2024, **34**, 2402071.
55 Y. Ran, M. Li, H. Zhao, J. Ren, Y. Sheng, G. Shao, Y. Wang and Y. Lei, *Adv. Funct. Mater.*, 2025, e10241.